Nanoscale

Accepted Manuscript

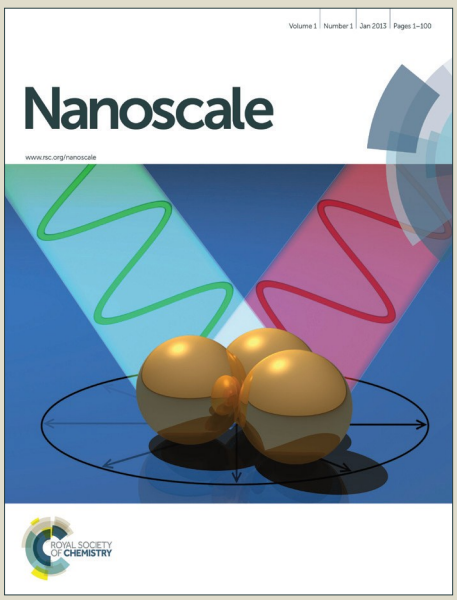

This is an *Accepted Manuscript*, which has been through the Royal Society of Chemistry peer review process and has been accepted for publication.

Accepted Manuscripts are published online shortly after acceptance, before technical editing, formatting and proof reading. Using this free service, authors can make their results available to the community, in citable form, before we publish the edited article. We will replace this *Accepted Manuscript* with the edited and formatted *Advance Article* as soon as it is available.

You can find more information about *Accepted Manuscripts* in the Information for Authors.

Please note that technical editing may introduce minor changes to the text and/or graphics, which may alter content. The journal's standard Terms & Conditions and the Ethical guidelines still apply. In no event shall the Royal Society of Chemistry be held responsible for any errors or omissions in this *Accepted Manuscript* or any consequences arising from the use of any information it contains.

ROYAL SOCIETY OF CHEMISTRY

www.rsc.org/nanoscale

Journal Name

Nanoscale

Dynamic Article Links ►

Cite this: DOI: 10.1039/c0xx00000x

www.rsc.org/xxxxxx

ARTICLE TYPE

Construction of three-dimensionally ordered inverse opal from nanofibers by soft-template approach: application to macro-mesoporous Li_2FeSiO_4/C composite for high-rate lithium-ion batteries

Donglin Li*, Yiyang Mao, Hong-Tuan-Hua Yong, Xiaoyong Fan*, Lei Gou, Miao Tian, Kun Zhao, Ru Sun, Wei Zhang, Guangqi Chen

Received (in XXX, XXX) Xth XXXXXXXXX 20XX, Accepted Xth XXXXXXXXX 20XX
DOI: 10.1039/b000000x

Exploring a new method to fabricate small-size nanofibers is essential to achieve superior performances for energy conversion and storage devices. Here, a novel soft-template strategy is developed to synthesize three-dimensionally ordered macroporous (3DOM) architecture constructed from small-size nanofibers. The effectiveness of nanofiber-assembled three-dimensional inverse opal structure as an electrode for high-rate lithium-ion batteries is demonstrated. The small-size Li_2FeSiO_4/C nanofibers with a diameter of 20-30 nm are grown by employing tri-block polymer P123 as a structure directing agent. Accordingly, the macro-mesoporous hierarchical 3DOM architecture constructed from Li_2FeSiO_4/C nanofibers is further templated from P123 for the nanofibers and polystyrene colloidal crystal array for 3DOM architecture. We find that thermal stability of the nanofiber morphology depends on the self-limited growth of nanocrystals in crystalline-amorphous hybrid. As a cathode for lithium-ion battery, the 3D hierarchical macro-mesoporous cathodes exhibit outstanding high-rate and ultralong-life performances with capacity retention of 84% after 1500 cycles at 5 C in the voltage window of 1.5−4.5 V, which is greatly improved compared with simple 3DOM Li_2FeSiO_4/C nanocomposite. More significantly, this soft-template method may be extended to other oxide nanofiber-based materials.

Introduction

One-dimensional (1D) nanomaterials are expected to play a key role in nanotechnology as well as to provide a light-insight to demonstrate high performance with applications ranging from capacitors, Li-ion batteries (LIBs) to solar cell. [1-3] In particular, small-size oxide nanofibers with a diameter of less than 30 nm are desirable as electrode materials for high-power LIBs. Most oxides are electrical insulators that limits charge transport at high charging/discharging current rates (C-rates), resulting in capacity losses due to incomplete utilization of active materials. For example, polyanion-type silicate Li_2FeSiO_4 (LFS) is a typically electrical insulating-oxide as a potential cathode material for LIBs.[4-14] LFS particles (with crystallite size >100 nm) severely suffered from sluggish kinetics due to its insulating character, leading to a poor rate capability.[5-7] In view point of the kinetics of electrode reaction in the LIB, for a lithium storage process it involves not only electron transport but also Li^+ ion diffusion in solid materials. In order to achieve superior high-rate capability, the charge transport kinetics needs to be enhanced. According to the diffusion formula $t = L^2/D$ (where t is the charges diffusion time, L is diffusion length, and D is the diffusion coefficient), the decrease in particle size from bulk to nanoscale leads to reduced ion/electron transport distance and increased surface area, then improving the rate performance.[5-12] However, nanoparticles have introduced new challenges, including higher surface area, low tap density and poor electrical properties due to the higher inter-particle resistance. The high surface area increases side reaction between active materials and electrolyte, and suffers from detaching from each other or self-aggregation during expansion/contraction cycling. This has encouraged the use of the specially nanostructured morphologies with one-dimensional (1D) nanostructured materials as an electrode for high-rate LIB,[10-11, 15-21], in particular, Li_2FeSiO_4 nanorods bonded with grapheme exhibits a superior rate-performances.[10-11] The rational design and synthesis of active materials with 1D nanostructures such as nanofibers or nanowires are important for high-power LIBs because of their vertical ion- and electron-transport properties and their ability to accommodate stress/strain induced by volume change in the electrodes.

Besides nanoscale morphological considerations, macroscopically ordered nanoporous structures such as nanowire arrays [22] or inverse opal structures, [23-26] particularly insulating oxides with a ordered nanoporous architecture is also essential to obtaining high-rate performances, because the ordered nanoporous structure can acts as a reservoir or transport channel within solid particles for the liquid electrolyte storage or transport, largely improving Li^+ ion diffusion rate through storing liquid electrolyte in solid particles. We thus envisioned that an interconnected three-dimensionally ordered macroporous (3DOM) architecture or inverse opal constructed from active nanocrystals / conductive carbon composite nanofibers with a small-size could endow the electrical insulate materials largely enhanced rate capability and cycling stability as an electrode for LIBs, which combines the merits of both nanofibers and ordered nanopores. Such a design offers several advantages over nanoparticle materials: (1) the nanosized primary particles completely encapsulated by a conductive carbon (C) are defined in the dense nanofibers, decreasing the surface area; (2) the continuous and 3D duel macro-mesopores facilitates electrolyte infiltration in addition to electron transfer through conductive

Nanoscale Accepted Manuscript

carbon, and in this way the active particles can access Li^+ ions more efficiently at high C-rates, compared with carbon-coated micrometer-sized particles; (3) the low tap density introduced when using nano-sized primary particles is partially solved, because of the space-efficient packing between the secondary macro-mesoporous particles as large as micrometers. Herein, by employing electrical insulator LFS as an example, we demonstrate a design and synthesis of hierarchical 3DOM architecture assembled with LFS/C nanofibes (3DOM-LFS/C-NF) via a simple sol-gel process followed by a post calcination step through using soft-template as a structure-directing agent (SDA). The target structure of a designed 3DOM nanocomposite is shown in Scheme 1e. The designed 3DOM architecture is constructed with the nanofibers consisted of a number of LFS nanocrystals coated with amorphous carbon. The effectiveness of the 1D nanofiber-assembled 3D inverse opal structure as an electrode for high-rate LIBs is demonstrated in this study.

To produce this type of hierarchical 3DOM architecture constructed from small-size nanofibers, three things are needed. The first is the fabrication of small-size nanofibers which will be used to build up interconnected macroporous frameworks. Traditionally, although many approaches have been developed to rationally design and synthesize nanowires or nanofibers, including electrospinning,[27-28] hydrothermal,[29-32] solution epitaxial growth (SEG),[33] supercritical fluid-liquid-solid (SFLS)[34], and vapor−liquid−solid (VLS) ,[16,35] the most of these methods are useful to growing the 1D nano-objects above 100 nm in diameter or need complex equipments. Although SEG and SFLS routes can produces small-size nanofibers, monocrystalline substrate or seeds is essential in these routes. It is difficult to utilize these methods to synthesize complex oxides and nanocomposite powders. On the other hand, it is also difficult to use these methods to form ordered nanoporous architecture constructed from nanofibers due to the incompatibilities on synthesis procedures of compositionally complex materials. There need great efforts on growing smaller-size 1D crystalline nano-objects such nanowire or nanofiber approximately less than 30 nm in diameter at reasonable cost and by versatile synthetic routes. Considering the solution self-assembly of a tri-block copolymer $HO(C_2H_4O)_{20}(C_3H_6O)_{70}(C_2H_4O)_{20}H$ (Pluronic P123, or P123) as a soft template for generating 2D hexagonally ordered mesotructures with cylindrical channels approximately 5-10 nm in diameters and sub-micrometers in length due to the formation of the columnar assemblies of cylindrical micelles in polar solvents,[36-40] we conceived that the desired small-size nanofiber could be templated by decreasing the diameters of the cylindrical assemblies to the nanoscale in surfactant solutions. To create LFS/C nanofibers building blocks for constructing 3DOM framework, the P123, which could be served as a SDA for nanofibers and also as a carbon source, is used to control LFS/C morphology at the nanoscale and to introduce a carbon phase into the LFS/C composite. The second is the construction of the 3DOM structure with LFS/C nanofibers. One simple route is the creation of interconnected macroporous (> 50 nm in diameter) architecture by using organic colloidal crystal array (CCA) as a template that is formed through controlled self-assembly of mono-disperse colloidal spheres during evaporation of a solvent. In a CCA, uniformly sized sphere are closely packed in predominantly face-centered cubic (fcc) crystalline lattice. Such an ordered CCA has interconnected interstitial octahedral (O_h) and tetrahedral (T_d) voids.[23] By replicating the interstitial voids same symmetry can be obtained. Meanwhile, by controlling the P123 cylindrical micelles, 1D nanofibers can be grown and further

The third criterion is the retention of the nanofiber-assembled 3DOM configuration during the crystallization of the materials. Generally, the crystallization of ordered mesostructured materials results in the collapse of their initial mesostructures due to Oswald ripening during crystal growth, because the size of designed mesostropic building block is less than that of resulted nanocrystals.[36-38] Herein, an amorphous carbon was introduced into the LFS material to control the growth of LFS nanocrystals in addition to providing an electron pathway, forming a LFS/C composite. Accordingly, the fabrication process of the 3DOM-

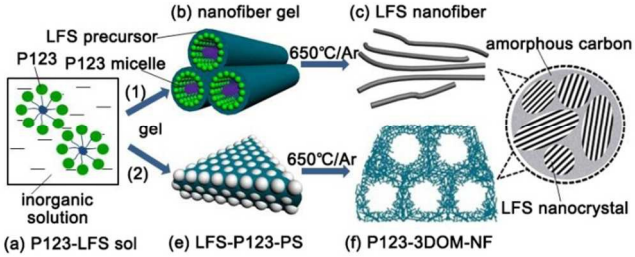

LFS/C nanofibers

.

Experimental

Mono-disperse polystyrene (PS) colloidal spheres approximately 200 nm in diameters were synthesized by polymerizing styrene as previous report.[41] The PS colloids were poured into a matrix and dried at 50
stacking up in ordered array as CCA templates. Ratio of Li: Fe: Si in the precursor was 2.1:1:1 (with little excess content of Li) for LFS/C nanocomposite. In a typical synthesis, 2 g of Pluronic P123 ($EO_{20}PO_{70}EO_{20}$) was dissolved in 80 ml of absolute alcohol

orthosilicate (TEOS), lithium acetate dihydrate ($CH_3COOLi{\cdot}2H_2O$) and iron(III) nitrate nonahydrate ($Fe(NO_3)_3{\cdot}9H_2O$) were added into above the solution, respectively, followed by stirring for 3 h, resulting in clear sol. For LFS/C nanofibes, the sol was poured into a dish to evaporate the solvent, forming a transparent slurry gel. After dried at 80℃, the gel was calcined in a quartz tube oven under flowing argon at 400℃ for 4 h, followed by calcination at 650℃ for 10 h. For three-dimensionally ordered macroporous architecture assembled from LFS/C nanofibers, the LFS-P123 sol was infiltrated completely into the CCA templates under vacuum. Then resultant hybrids were dried at 50℃, followed by a similar heat-treatment to the nanofiber preparation.

The morphologies of the materials were observed using field-emission scanning electron microscopy (FESEM, Hitachi S-4800). Crystalline or amorphous phases were investigated by an X-ray diffraction (XRD, Bruker D8A A25 X) with Cu Kč radiation and a high-resolution transmission electroscope (HRTEM, FEI Tecncnai F30). Raman spectra were collected in the 500–3500 cm^{-1} range with a Raman microspectrometer (Renishaw inVia) equipped with an Ar laser (wavelength 514.5 nm). Carbon contents were measured by a thermal gravimetric analysis (TGA).

The cathodes were prepared by casting a slurry consisting of 80 wt% of active materials, 15 wt% of carbon black and 5 wt% poly vinylidene difluoride (PVDF) as a binder onto an aluminum foil. The electrode thicknesses of the cathodes were designed to be 70 μm for all of cathodes. After drying the cathodes at 100 ℃ for 16 h, coin-type cells were assembled in an Ar-filled glove

Nanoscale Accepted Manuscript

This journal is © The Royal Society of Chemistry [year]

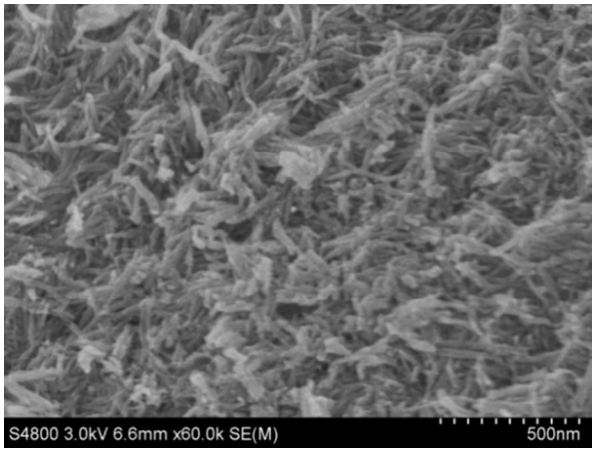

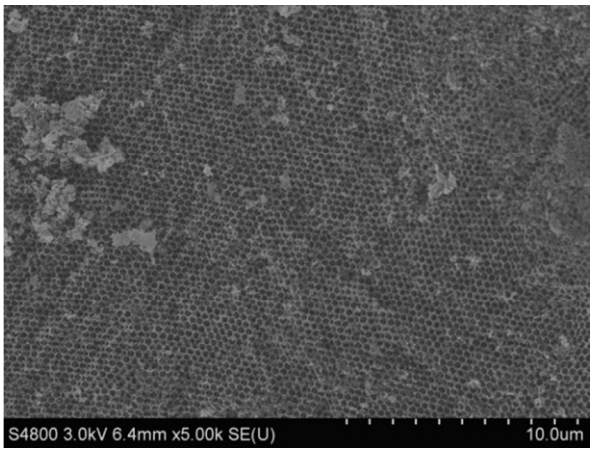

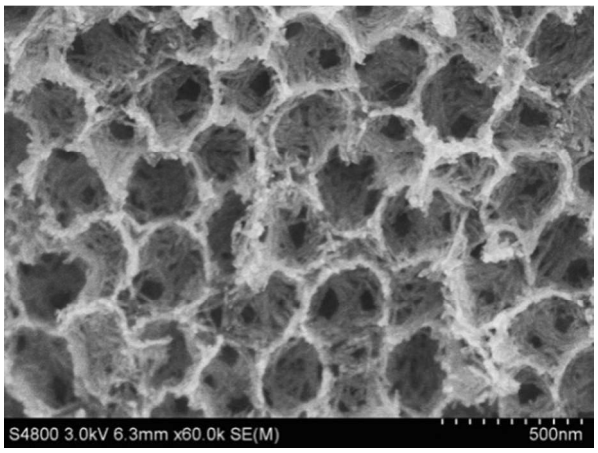

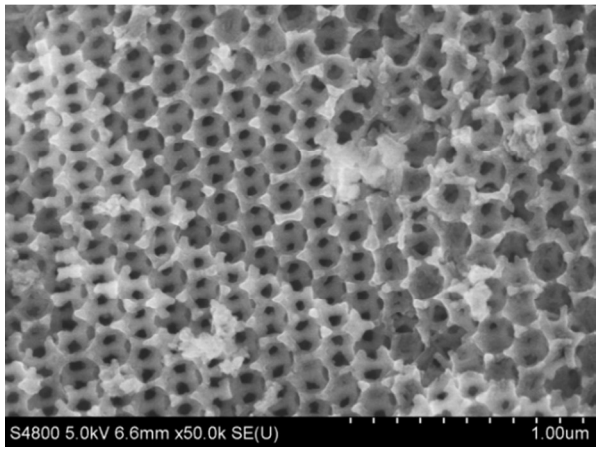

Nanoscale Accepted Manuscript

Cite this: DOI: 10.1039/c0xx00000x

www.rsc.org/xxxxxx

ARTICLE TYPE

Results and discussion

When placed in a block-selective solvent, the block copolymers assemble into a variety of different morphologies that are influenced by polymer molecular weights and block ratios, with a further control possibility through the manipulation of environmental conditions such as temperature, solvent, and concentration. The tri-block copolymer P123 is usually used as a template to direct ordered mesoporous materials due to the formation of the columnar assemblies of cylindrical micelles in aqueous solution.[36-40] In order to obtain the desired LFS/C nanofibers (LFS/C-NF) with a small size, it is required a method to create P123-LFS organic-inorganic hybrid nanofibers where the LFS precursor resides outer layer of P123 micelles (Scheme 1b). To explore the feasibility of this approach, we performed the studies on the hybrid cylinders derived from the P123 and inorganic agents. The nanofibers are prepared via sol-gel and subsequent calcination processing, as shown in Scheme 1a-c and also described in detail in the Experimental section. With different from previous ordered mesoporous process,[36] we prepared the sols containing P123 and LFS precursors in the absence of HCl, then evaporated the solvent at room temperature, forming a transparent slurry-like gel. After it was dried at 80℃, followed by the calcination at 650℃, the desired nanofibers were successfully obtained.

From the FESEM images of the samples, it could be clearly observed that the samples exhibited a fiber-shaped morphology and uniformly mesopores (Fig. 1a). Importantly, the nanofibers exhibit uniform-size distribution in the FESEM images. The average diameter and length of the resulting nanofibers are about 25 nm and 200 nm, respectively, possessing a narrow size distribution. It is noted that the small-size nanofibers aggregate easily with each other if the gel is heated at 100℃ for a fast drying, as shown in Fig. 1b. In fact, it is difficult to completely control the agglomeration of the nanofibers because many factors, such as temperature, solvent and inorganic ions, etic, have complex effects on the drying procedure of the gel. XRD patterns from the synthesized materials indicates that the primary reflection peaks can be indexed to a monoclinic structure with a space group $P2_1/n$ according to the results reported by Nishimura et al.,[42] as shown in Fig. S1a. However, noticeable changes in the relative peak intensities occurred with the emergence of weak peaks at 2θ=36.69° and 42.59°, tentatively attributed to the overlapping peaks from both a little $Li_2Fe_3O_4$ impurity and LFS nanocrystals. The $Li_2Fe_3O_4$ impurity fully disappears by improving homogeneity of the gel in the sol-gel process, but very weak peaks from $Li_5Fe_5O_8$ are detected (Fig. S1 b). The LFS nanocrystals are approximately 8±3 nm in size according to Scherrer method from (111), (202) and (020) reflections for the sample calcined at 650℃. A high resolution transmission electronic microscopy (HRTEM) image (Fig. S2) taken on the nanofibers displays clear crystal planes, which shows lattice fringes with basal distances of 0.270 nm, corresponding to (-103) plane of LFS crystal, and an amorphous carbon phase covers the surface of the LFS nanocrystals, revealing that the nanofibers are consisted of smaller LFS nanocrystals and amorphous carbon.

The amorphous carbon layer is also identified by Raman spectrum. Fig. 2a shows the Raman spectrum of as-produced LFS/C-NF composite. The presence of the typical G-band at 1598 cm^{-1} and D-band at 1350 cm^{-1} usually correspond to the E_{2g} nodes of graphite and disordered carbon, respectively. [43] The large broadening of the full width at half maximum (FWHM) of D band is associated with the disordered carbon structures,[44-47] which reveals more amorphous characteristic of the carbon phase than that of pure graphitic carbon. Considering that the G band is associated with graphitic sp^2 carbon structures, [48] the intensity ratio I_D/I_G (~0.75) of D band over G band, which is often used to correlate the structural purity of graphite [44-45], also indicates that the carbon phase is composed of mainly nanocrystalline graphite and disordered carbon atoms [41-43]. The results from the Raman analysis are consistent completely with the HRTEM observations. These results indicate that the LFS/C NFs with a diameter less than 30 nm can be synthesized by sol-gel route using P123 as a SDA, which represents a novel approach on synthesizing small-size nanofibers.

Next, with confidence in our ability to create LFS/C nanofibers, we further use polystyrene (PS) CCA as a template to construct the 3DOM architecture assembled from the LFS/C nanofibers so as to overcome the problem of agglomeration of nanofibers. For this purpose, the mono-disperse PS spheres with a diameter of 200 nm crystallize into close-packed arrays with face-centered cubic (FCC) symmetry. The PS CCA template was immersed completely into the LFS/P123 sol under vacuum. The LFS/P123 component occupying the T_d and O_h voids builds up the interconnected 3D macropores. The resultant hybrids were dried at 80 ℃, followed by heat treatment in an inert atmosphere of argon at 400 ℃ for 4 h for removing the partial organic agents, then continuously calcinated at 650 ℃ for 6h. Thus, 3DOM LFS/C-NF micrometer-size particles or flakes with 3D-interconnected hierarchically porous networks were obtained (Fig. 1 c). For all the samples, large fractions (more than 90 % of particles by FESEM images) of the calcined samples possess ordered macroporous structure in 3D space over a range of tens of micrometers. A magnified FESEM image reveals that the porewalls of 3DOM structure are constructed by randomly oriented nanofibers approximately 20-30 nm in diameter, which are interconnected with each other to form a mesoporous porewalls of 3DOM architecture (Fig. 1d). Therefore, there are two kinds of pores in the micrometer sized particles. One is 3D ordered macropores with a diameter of 140 nm, another is mesopores between the nanofibers within the walls of the macropores, thus keeping a 3D hierarchical duel-nanoporous networks.

Although the material heated at 400 ℃ appears to be amorphous based on XRD measurement (Fig. 3a), they are subsequently crystallized in a controlled way by a calcination at 650 ℃. All of the diffraction peaks of the samples calcined at 650 ℃ is fully indexed to monoclinic $P2_1/n$ structure of the LFS crystal (Fig. 3b). The HRTEM images taken nanofibers shows that the nanofibers are composed of LFS nanocrystals and amorphous carbon (Fig. 4). It indicates that a small amount of the amorphous carbon layer with a thickness of 1 to 4 nm is coated on the surface of LFS nanocrystals, forming LFS/C composite nanofibers. The HRTEM images show uniformly dispersed LFS

Nanoscale Accepted Manuscript

nanocrystals, with a narrow distribution of nanocrystal sizes between 3 and 9 nm. The average size of the LFS nanocrystals is about 7 nm, in agreement with the XRD results.

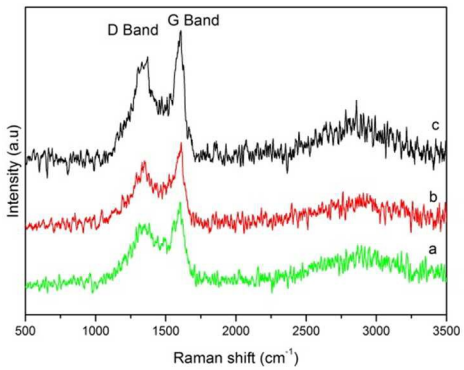

Fig. 2 Raman spectra of the Li_2FeSiO_4/C composites. (a) LFS/C-NF, (b) 3DOM- LFS/C-NF, and (c) 3DOM-LFS/C.

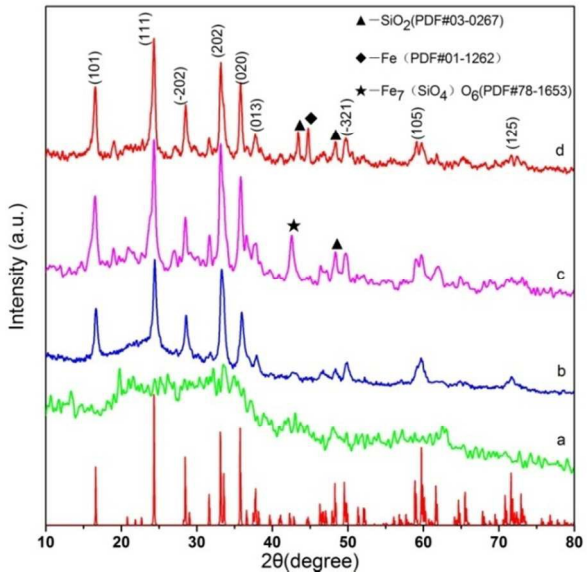

Fig. 3 XRD patterns of the nanofiber-assembled macroporous Li_2FeSiO_4/C composites (3DOM-LFS/C-NF) cacined at various temperatures. (a) 400℃, (b) 650℃, (c) 700℃, (d) 750℃. Bottom is ICSD#246132 pattern of Li_2FeSiO_4.

For comparison, 3D ordered macroporous LFS/C nanocomposite (3DOM-LFS/C) was also synthesized by PS CCA as a SDA using a resol in place of the P123 as a carbon source. XRD measurement shows that all reflections can be index to monoclinic $P2_1/n$ structure of the 3DOM-LFS calcined at 650℃ (Fig. S3), the size of nanocrystals is similar to the 3DOM-LFS/C-NF. The macropores have a diameter of 140 nm estimated from the FESEM images (Fig. 1e). The thickest thickness of the porewalls is approximately 85 nm occupied in the T_d voids of the CCA, in agreement with theoretical data (82 nm).[23] The FESEM image shows that no secondary irregular mesopores were observed in the poreswalls of 3DOM structures, achieving fully densely sintered ceramics. In contrast, the thickness of the porewalls is approximately 20-30 nm for the 3DOM-LFS/C-NF because they contain nanofiber-packed mesoporores. The comparable intensity and shape changes of the D and G bands of the Raman spectra should be associated with the structural changes. [42-44] For the 3DOM-LFS/C, LFS/C-NF and 3DOM-LFS/C-NF composites, the FWHM of G band and I_D/I_G ratio (0.76, 0.75, 0.75) do not almost change (Fig. 2), which implies the structure of carbon phase is almost similar in these samples, exhibiting an amorphous state containing partially graphitic nanocrystals. According to TG analysis, the carbon content in as-synthesized 3DOM-LFS/C-NF, LFS/C-NF and 3DOM-LFS/C composites are 10.3%, 7.4%, and 13.7%, respectively.

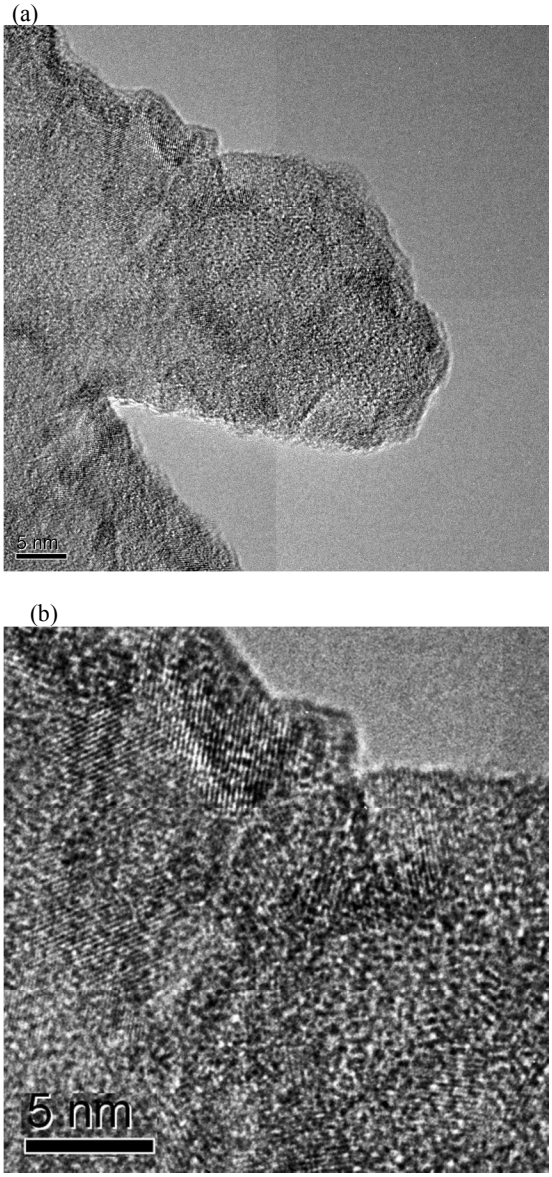

Fig. 4 TEM (a) and HRTEM （b） images of 3DOM-LFS/C-NF composites cacined at 650℃.

Since the LFS nanocrystallites coated with an amorphous carbon are sintered to fully dense LFS/C composite nanofibers, such a hierarchical structure with 3-D interconnected nanoporous networks is expected to retain a relatively stable micro- or nano-architecture during charge-discharge (contraction-expansion) cycles. The present macro-mesoporous architecture is fundamentally different from previous reports of nanostructured electrode materials. Firstly, the active LFS nanocrystals are integrated in a dense composite nanofiber which can be used to

Nanoscale Accepted Manuscript

build up 3DOM architecture, fast transporting electrons. Secondly, the macro-mesopores inside the micrometer-size particles are well-defined, effectively transporting and storing liquid electrolyte. Finally, the well-defined void spaces do not decrease the volumetric capacity, because they are designed to be mostly occupied in lithiated state. Such a design integrates the merits of both 1-D nanofiber and nanopore into micrometer-size particles.

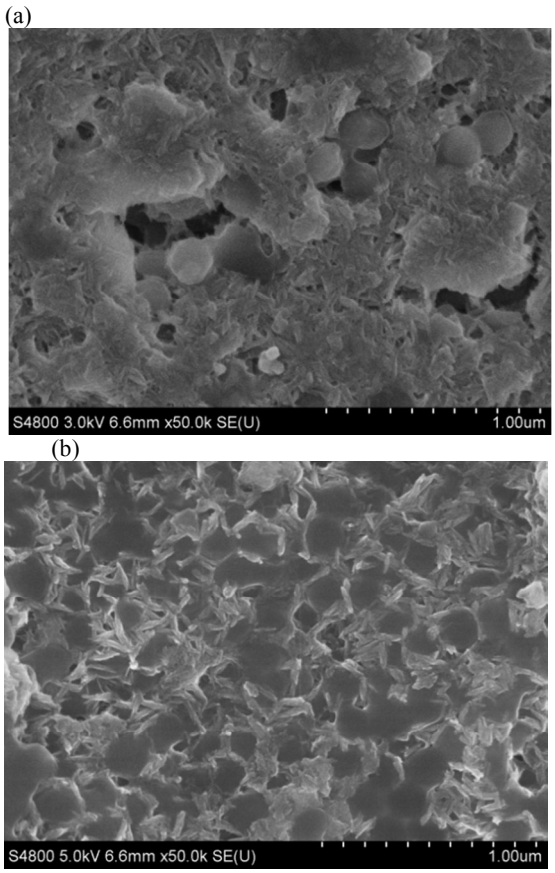

Fig. 5 FESEM images of the LFS/P123-PS gels heated at (a) 100 ℃ and (b) 200 ℃

To further understand the formation mechanism of nanofibers-constructed 3D macro-mesoporous architecture, we had carefully examined the nanostructures of the materials during heating procedure. After dried at 80℃, the LFS-P123-PS gels were heated in the temperature range of 100-750℃. Nanofiber morphology was examined at 100℃ and retains up to 750℃. In the temperature range of 100 - 200 ℃, these nanofibers resides the voids between PS CCAs, as shown in Fig. 5. These findings confirm that the nanofibers in the walls of the macropores originate from P123 micelles, while the PS spheres does not affect the LFS-P123 gel nanofiber morphology during the processing of filling LFS-P123 sols into the PS CCAs, and nanofiber formation can still occur from the LFS-P123 sol. As is similar to the case on the LFS/C-NF, the nanofibers originate from the P123 micelles in the LFS-P123 sol with or without PS CCAs. The nanofiber morphology retains to 700℃ (see below). Generally, the crystallinity and morphology of the materials are closely associated with the calcining temperature and annealing time during the crystallization process. For the LFS-P123-PS hybrid gels, the calcination process at 650℃ in an argon leads to the formation of a highly hierarchically macro-mesoporous LFS/C framework constructed from the nanofibers, as shown in the FESEM image (Fig. 1d). The annealing time at this temperature does not markedly influence the crystallinity, because we did not observe any significant differences in the crystallinity of the material heated at 4 h and 40 h, respectively. Calcination at 700 ℃ for 4h did not result in apparent growth of LFS crystalline domains, but a little of secondary crystalline phases were observed in the XRD measurement, and macro-mesoporous nature of the LFS/C framework remains preserved (Fig. S4 a). When calcining the as-prepared gels at 750℃, a weak peak of iron (Fe) nanocrystals was detected in the XRD pattern (Fig. 3), and larger particles (around 200 nm) were observed in the FESEM images. The LFS and iron crystal growth at 750℃ is accompanied by the collapse of porosity (Fig. S4 b). These findings show that the calcination at 650℃ constitutes the optimum calcination conditions for the nanoscale LFS materials. On the base of these results, the formation mechanism of the nanofiber-constructed macro-mesoporous architechture can be explained as follows. In a first step, when dissolved in an ethanol solvent, the block copolymers assemble into cylindrical micelles which incorporates with the hydrolysis of LFS precursor, producing bundles of cylindrical micelles about 20-30 nm in diameter, and forming the nanofiber morphology (Scheme 1a-b). The composition of the hybrid is inhomogeneous at the mesoscale in the assembling hybrid. It should be mentioned that, unlike the processing of synthesizing ordered mesoporous materials in the presence of HCl, [36] the LFS-P123 hybrid nanofibers in the present study are obtained in the absence of HCl, and the concentration of P123 is lower than that needed for the formation of ordered lyotropic phase. [49] The co-organization of organic and inorganic species was thought to be the key factor for the mesostructural materials. In the case of the hexagonally ordered mesoporous structure, the HCl are essential to the assembly of P123 micelles-inorganic agencies into micrometer-sized assemblies for ordered mesoporous materials due to the hydrogen-bonding or Columbic interactions of nonionic block copolymer with inorganic agencies under acidic conditions through cations and anions, [50-51] it means that the HCl helps with forming ordered mesostructured assemblies with a diameter as large as micrometers. On the contrary, the small-size assemblies with a diameter as small as 30 nm can form due to weakening H-bond reaction between the micelles in the case of lower concentration of P123 as well as in absence of HCl in the sol. We believe that the synergetic effect of those two species is essential to controlling the different mesostructual morphologies. In the second step, the as-prepared nanofiber gel was calcined to crystallize the LFS with the release and *in situ* carbonization of organic compounds during heating procedure. After the organic fragments have been carbonized through the calcination process under an Ar atmosphere, an inorganic oxide-carbon composite solid will be produced. When the organic carbon source P123 is converted to an amorphous carbon above 500℃, multicomponent oxides produces phase separation at the nanoscale, forming nano-sized （Li, Fe, Si）domains and amorphous carbon phase during heating. With increasing the calcination temperature up to 650 ℃, the LFS nuclei grow in-situ into LFS nanocrystals. For LFS crystals to nucleate and grow, Li^{+} and Fe^{2+} ions must diffuse during the crystallization of the amorphous hybrid gel, but the amorphous carbon forms a diffusion barrier which hinders further growth of LFS nanocrystals, resulting in small-size LFS nanocrystals. The resulting LFS nanocrystals do not grow apparently with annealing time in a given temperature below 700 ℃, thus it is difficult to further grow into larger crystallites. This

Nanoscale Accepted Manuscript

This journal is © The Royal Society of Chemistry [year]

conclusion results from the fact that the crystal growth is limited by the consecutive formation of amorphous carbon around LFS nanocrystals. This kind of self-limited growth is reported in other silica-based and phosphate-based glass ceramics, [52-55] i.e., a typical amorphous-crystalline structure. As a result of the self-limited growth, the nanocrystal-amorphous carbon composite retains a good thermal stability due to limited Ostwald ripening during crystal growth in the temperature range of less than 700 ℃. If a higher temperature is further supplied, however, the carbothermal reduction between the LFS and carbon makes LFS nanocrystals dissolve and carbon phase pyrolyzes, resulting in metallic iron [8] and leading to a collapse of the nanofiber morphology and 3DOM architecture.

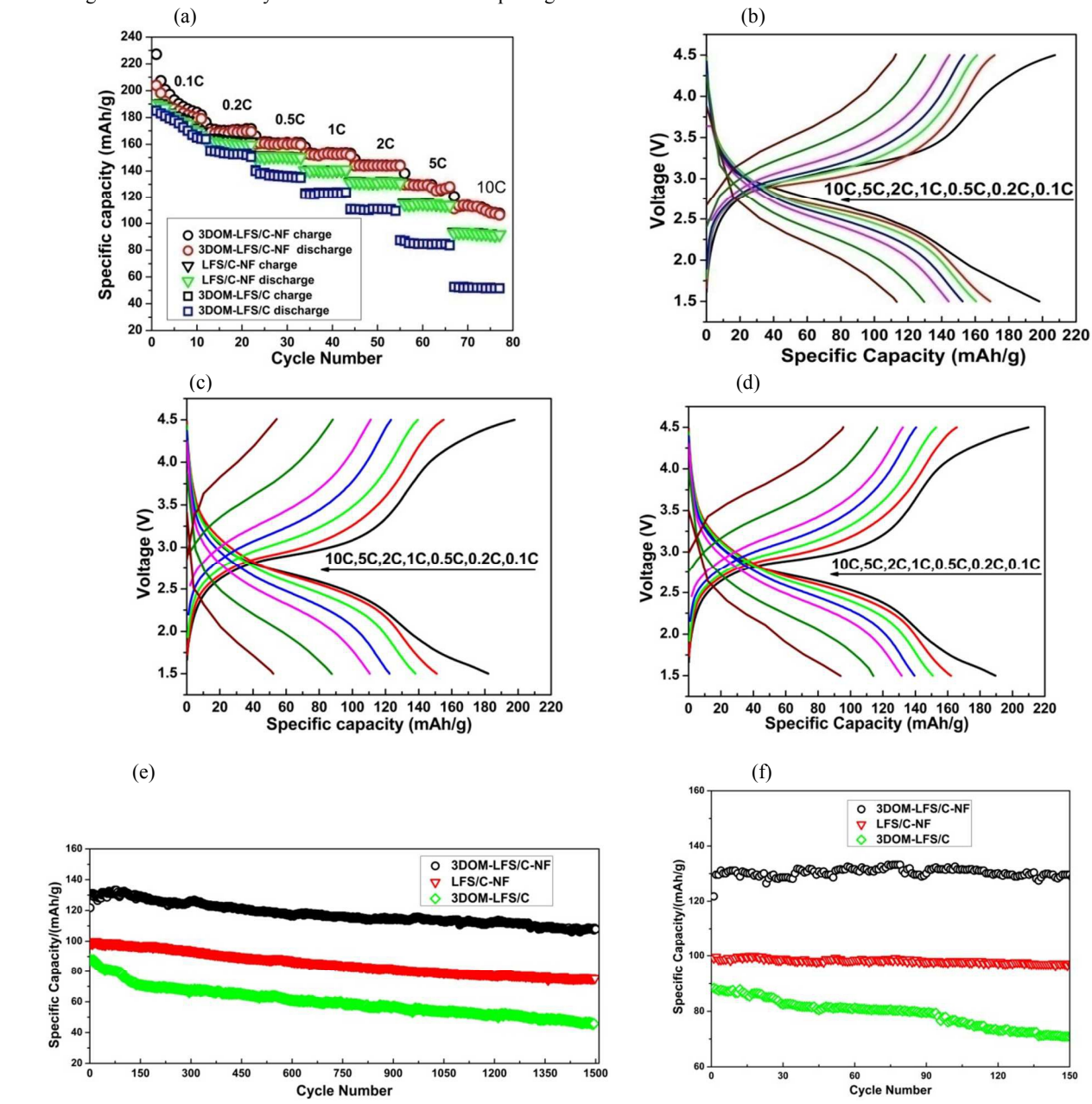

Fig. 6 Rate performances of the hierachical Li_2FeSiO_4/C (LFS/C) composites cacined at 650℃ at various current rates between 1 and 10 C in the voltage window of 1.5~4.5V at 28℃. (a) Rate cycling performances of the samples. (b-d) Charge/discharge voltage profiles of (b) 3DOM-LFS/C-NF, (c) 3DOM-LFS/C, and (d) LFS/C-NF, (e) Ultra-long cycling performances of the materials calcined at 650 ℃ at 5C, (f) Cycling performances in the early 150 cycles.

To verify the effects of the porous structures on the rate-performances of the cells, a comparison among the 3DOM-LFS/C-NF, LFS/C-NF and 3DOM-LFS/C cathodes is presented. Fig. 6 shows the rate performances of the 3DOM-LFS/C-NF, LFS/C-NF and 3DOM-LFS/C cathodes. Because the electrode thicknesses of the cathodes were designed to be same (70 μm) for all of cathodes, the effects of electrode thickness on rate performance can be ignored. The loading mass densities of active materials on the 3DOM-LFS/C-NF, LFS/C-NF and 3DOM-LFS/C cathodes are 1.43, 1.76 and 1.68 mg $cm^{-2,}$ respectively. The hierarchically macro-mesoporous 3DOM-LFS/C-NF cathode exhibits superior rate performance compared with the 3DOM-LFS/C. One obvious improvement in rate capability is that 3DOM-LFS/C-NF cathode exhibits noticeably slower fade of

Nanoscale Accepted Manuscript

capacity at higher C-rate. Although all of three cathodes exhibit a fading trend with increasing C-rates, the 3DOM-LFS/C-NF exhibits slight drops in discharge capacity. In contrast, the 3DOM-LFS/C shows larger fade at higher rates (Fig. 6a). For example, the 3DOM-LFS/C shows notable drops in discharge capacity upon stepwise C-rate increases from 1C to 10 C, while the 3DOM-LFS/C-NF cathode exhibits gradual fade in capacity. The 3DOM-LFS/C-NF can still deliver a discharge capacity of 117 mAh g^{-1} at a C-rate as large as 10 C after 70-80 cycles, more than twice that of the 3DOM-LFS/C cathode (52 mAh g^{-1}), which indicates to a capacity loss only 0.9 % per cycle from initial discharge capacity of 180 mAh g^{-1} in 10th cycle at 0.1 C, corresponding to capacity retention of 65 %. In contrast, the discharge capacity of the 3DOM-LFS/C drops dramatically from 175 mAh g^{-1} in the 10th at 0.1 C to 52 mAh g^{-1} at 10 C, which suffers a capacity fading rate of 1.8 % per cycle, corresponding to capacity retention of 30 %. Another improvement in rate performances is that the 3DOM-LFS/C-NF cathode exhibits the smaller voltage hysteresis at higher rates （Fig. 6 b）, while the 3DOM-LFS/C cathode exhibits the largest hysteresis (Fig. 6c). Generally, the voltage hysteresis was growing noticeably with faster C-rates, but the 3DOM-LFS/C-NF exhibits noticeably smaller hysteresis compared with the 3DOM-LFS/C cathode. For example, the discharge plateau voltages fade gradually toward lower potential for the 3DOM-LFS/C-NF at high C-rates, while the 3DOM-LFS/C exhibits more rapid drop of the plateaus voltage. Specifically, the flat plateau disappears at 10 C for 3DOM-LFS/C, while it is obviously distinguished for the 3DOM-LFS/C-NF cathode. These results imply that the electrochemical polarization in the 3DOM-LFS/C-NF cathode is suppressed compared with the 3DOM-LFS/C, indicating that the charge transport kinetics is improved in the 3DOM-LFS/C-NF. This depolarization with high charge transport kinetics is identified by cyclic voltammetry measurements, as shown in Fig. 7. Compared with the 3DOM-LFS/C cells, the redox reaction of the Fe^{2+}/Fe^{3+} in the 3DOM-LFS/C-NF cathode is down-shifted by about 0.1 V (located at 3.15/3.05) even if scanning rates are slowly, indicating the low overpotential due to the improvement of charge transport kinetics for the 3DOM-LFS/C-NF and the LFS/C-NF cells even at a low scanning rate of 0.05V s^{-1}. It is should be pointed out that the LFS/C-NF composites exhibit unstable rate performances depending on the degree of nanofiber aggregation. Well-dispersed nanofibers possess comparable properties to the 3DOM-LFS/C-NF cathode (Fig. 1a, Fig. 6a and Fig. 7), while the relatively seriously aggregated LFS/C-NF shows relatively poor rate performances due to the barriers to electrolyte access (not shown here). The improvement in rate capability is dramatic by constructing macro-mesoporous architecture from nanofibers. As a result, the 3DOM-LFS/C-NF cathode may deliver a higher energy than the 3DOM-LFS/C cathodes at high C-rates. Although the rate performance is similar to our previous LFS/Fe_7SiO_{10}/C or LFS/Fe/C nanocomposites, [7-8] the apparent specific capacity of present 3DOM-LFS/C-NF cathode is higher because of decreasing the contents of inactive phase such as Fe and Fe_7SiO_{10} in the electrodes.

It is noted that the LFS/C-NB containing a small quantity of $Li_2Fe_3O_4$ impurity shows additional oxidation peak at 2.95 V in the CV curves during first and second cycles at different scanning rates from 0.05 to 0.5 mV s^{-1} (Figure S7a). Taking into consideration the XRD analysis (Figure S 1a), this peak may be associated with the $Li_2Fe_3O_4$ impurity. Because sol-gel derived silica-based oxides usually exhibit a phase separation, $Li_xFe_yO_z$ and containing-silicon impurities have been found in LFS materials.[7, 56-58] The Li_2SiO_3 and Fe_7SiO_{10} can improve rate performance of LFS cathodes,[7,56] while electrochemically active α −$LiFeO_2$ can contribute an additional capacity to the cathodes. Typically, Zhou and Vullum-Bruer et al. reported that the $Li_2Fe_xSiO_4$/C containing α −$LiFeO_2$, which is exhibits 250 mAh g^{-1} in the voltage window of 4-1.5 V, [59] imposes significant effects on the discharge capacity in the range of 2-1.5 V [58]. The present LFS/C-NF composite containing $Li_2Fe_3O_4$ shows additional oxidation/reduction peaks during initial and second CV cycles, which disappear from third cycles. This is consistent with the discharge curves that seem to exhibit additional capacity during initial and second cycles but ambiguous from third cycle in the voltage window of 2-1.5 V at 0.1 C, as shown in Fig. S5. These phenomena occur during the initial stage of the reaction. It is perhaps transient in nature and not present during sequent cycles. Obviously, the effects of the $Li_xFe_yO_z$ on the charge/discharge are complex. It needs to be further investigated.

In order to further understand the charge transport kinetics for the high-rate charge/discharge performances of the 3DOM-LFS/C-NF cathode, electrochemical impedance spectra (EIS) were measured after 50th-cycle at 2C. Fig. 8 presents the Nyquist plots of the Li_2FeSiO_4/C cathodes measured during 50th cycle. The AC impedance Nyquist plot showed a semicircle at high frequencies, which is assigned to the charge transfer impedance at the electrode-electrolyte interface (R_{ct}), and a straight line in the low-frequency region, which is attributed to the semi-infinite diffusion of Li ions in the LFS electrodes (R_e). The R_{ct} and R_e show lowest values for the 3DOM-LFS/C-NF, but highest for the 3DOM-LFS/C cathode. Clearly, the transport kinetics of 3DOM-LFS/C-NF cathode is improved compared with the other cathodes. It is noted that the R_t and R_e values of LFS/C-NF cathode are close to the 3DOM-LFS/C-NF, as is consistent with their high-rate charge/discharge performances. The Li^+ diffusion coefficients in the solid calculated based on the EIS measurements [56] are 7.62×10^{-13}, 4.54×10^{-13}, 2.67×10^{-13} $cm^2\cdot s^{-1}$ for the 3DOM-LFS/C-NF, LFS/C-NF and 3DOM-LFS/C, respectively, on the same order of 10^{-13}, which are consistent with the results from the CV measurements[5] (Figs S6-S8, Table S1). Thus, the EIS measurements imply that the superior rate-capability of the 3DOM-LFS/C-NF cathode originates from uniformly smaller-size nanofiber morphology and macro-mesoporous structure.

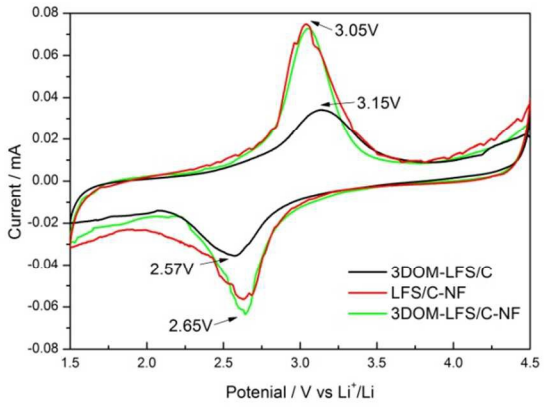

Fig. 7 Cyclic voltammetry (CV) of the 3DOM-LFS/C-NF compared with LFS/C-NF and 3DOM-LFS/C cathodes.

Although the LFS/C-NF cathode shows a comparable rate-performance to the 3DOM-LFS/C-NF at higher C-rates, the latter exhibits a superior long-life cycles to the former. To further clarify the effects of the nanostructures on the cycleability at higher C-rates, the long-life cycles of the LFS cathodes with different nanostructures were then tested at higher C-rate of 5C

Nanoscale Accepted Manuscript

This journal is © The Royal Society of Chemistry [year]

(Figure 6 e, f). The 3DOM-LFS/C-NF exhibits a best higher capacity under same test conditions during long-life cycling performances. When cycled at 5C in the voltage window of 1.5−4.5 V, the initial discharge capacity of the 3DOM-LFS/C-NF cathode is 128 mAh g^{-1}, higher than those of LFS/C-NF (98 mAh g^{-1}) and 3DOM-LFS (86 mAh g^{-1}). However, noticeable decrease of 10 mAh g^{-1} in capacity occurs under directly charging/discharging the LFS/C-NF cathode at 5C (Fig. 6e), compared with the measurement result at 5C at variable C-rates from slow-rate 0.1C to fast-rate 10C (Fig. 6a). This is perhaps dependent of the charge/discharge steps. For the charge/discharge cycles at variable C-rates from low-rate to high-rate, the electrolyte can penetrate sufficiently into mesopores among the aggregated nanofibers at lower C-rates, almost all active material take part in electrochemical reaction, exhibiting higher capacity. In contrast, directly charging/discharging the LFS/C-NF composite at high-rate, the cell exhibits relatively lower capacity at same C-rate. The disadvantage of the aggregated nanofibers is improved by macro-mesoporous structure in the 3DOM-LFS/C-NF cathode. On the other hand, the aggregation of nanofibers has an effect on the capacity, the electrode with nanoporous structure constructed from well-dispersed nanofibers (Fig. 1a) delivers relatively high capacity due to relatively full utilization of active materials during electrochemical reaction, compared with relatively seriously aggregated nanofibers (Fig. 1b). After 1500 cycles, the capacity retention of 3DOM-LFS/C-NF is 84.5%, while the original capacity retentions of the LFS/C-NF and 3DOM-LFS cathodes are only 76.1% and 52%, respectively. Moreover, unlike in the case of the 3DOM-LFS/C-NF and LFS/C-NF cathodes which show relatively stable **cycleability**, the capacity of the 3DOM-LFS/C cathode starts fading very rapidly from 86 mAh g^{-1} in the 20th cycle to about 75 mAh g^{-1} in the 100th cycle, **thereafter,** gradually fading to reach 46 mAh g^{-1} after 1500 cycles, indicating that the microstructure of the 3DOM-LFS/C cathode is not stable during high-rate charge/discharge cycles.

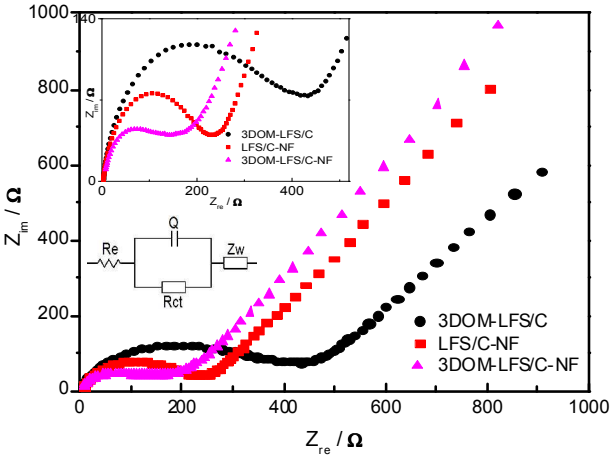

Fig. 8 Nyquist plots of the as-prepared samples measured at ~50% state of charge (~3.2V) during the 50th cycle at 20℃.

In the present works, the morphology of active materials has an important effect on the rate-performances of LFS cathodes. The 3DOM-LFS/C-NF exhibits superior electrochemical properties compared with 3DOM-LFS/C composite. Considering that the carbon phase exhibits similar amorphous structure (mixture of nanoscale graphitic order and disorder carbon), all of cathodes should possess similar electronic conductivity at the nanoscale. Thus, the superior electrochemical properties of the dual macro-mesoporous architecture constructed from LFS/C composite nanofibers can be attributed to several unique features compared with the other LFS/C nanocomposites in present work. Firstly, the active LFS nanocrystals (3-7 nm) coated with amorphous carbon are sintered into dense nanofibers with small diameters (20-30 nm) in which the conductive carbon offers continuous electron transport pathway within the porewalls of the 3D macro-mesoporous architecture. Because the structure and content of carbon in the 3DOM-LFS/C-NF composite is similar to the other LFS/C composites, the effects of the carbon phase on rate-performance are same for three kinds of cathodes. Secondly, the macro-mesoporous channels provide rapid electrolyte transport pathways and storage reservoirs in the solid electrode. When liquid electrolyte fill with 3D macro-mesopores, the micromerter-sized LFS/C particles become LFS/C nanofibers-electrolyte 'hybrid' micrometer-size particles composed of ion-conductive electrolyte and insulating LFS/C nanofibers (10^{-13} mS cm^{-1}). Since the specific conductivity of the electrolyte is in the range of 10^{-2}-10^{2} mS cm^{-1}, [57] the average value D_{ave} of the ion diffusion coefficient of this lithium-ion conductor-insulator 'hybrid' particles rapidly increases, even near to that of the electrolyte with decrease of the nanofiber-size and increase of the macro-mesoporous LFS/C particle size according to the diffusion formula $t = L^2/D$. Thus, lithium ion transport pathways greatly facilitate the ion diffusion kinetics at least from 1C to 10C, resulting in relatively high portion of utilizing active materials at high C-rates. In contrast, electrochemical lithiation / delithiation reactions in 3DOM-LFS/C cathodes is not fully complete due to the thicker porewalls (80 nm), resulting in an inferior rate-capability at high C-rates. Finally, and eventually most importantly, the hierarchical 3DOM in the 3DOM-LFS/C-NF cathode confines the LFS/C nanofibers in the walls of the macropores, completely avoiding agglomeration of the nano-objects, and limiting self-aggregation of active materials over repeated cycling and improving the impregnation of electrolyte into the electrodes. Moreover, the stable micro-nanostructure can accommodate stress/strain induced by the volume variations during Li^+ extraction/insertion cycles, which guarantee the effective electrical contact upon prolonged cycling. Thus, the 3DOM-LFS/C-NF exhibits more excellent long-life cycleability than the LFS/C-NF.

It is worthy noted that the LFS/C-NF composite is subtle because it is not easy to control the dispersion of the nanofibers during material synthesis. The LFS/C-NF composite with well-dispersed nanofibers is comparable to the 3DOM-LFS/C-NF, while seriously aggregated LFS/C-NF shows relatively poor properties at high rates (not shown herein). With this 3D maro-mesoporous architecture consisted of nano-sized primary active particles coated by amorphous carbon, the disadvantage of the nanofibers can be overcome. Also, nanofiber-assembled three-dimensionally macroporous secondary particles with several macrometers in size maintain the high surface but overcome the low tap density of nanoparticles. Such hierarchical architecture of nanofibers together with the synergistic effect nanofiber and nanoporous particles with micro-sizes makes a prominent contribution to excellent electrochemical performance.

It should be pointed out that the Li_2FeSiO_4 is a promising cathode material that may undertake the extraction/insertion mechanism of two lithium ions per formula unit, which is a multielectron charge transfer (Fe^{2+}/Fe^{4+} redox couple) process, thus leading to the theoretical capacity of 332 mAh g^{-1}. In our present and previous experiments,[7-8] the discharge capacity of nanostructured LFS exhibits capacity of 180-200 mAh g^{-1} within the voltage window of 1.5-4.5 V in the several of the early cycles at 0.1 C (Figure 6a), corresponding to more than one lithium

Nanoscale Accepted Manuscript

extraction/insertion. In fact, several of research groups demonstrated a fully reversible extraction/insertion of two lithium ions in the LFS/C nanocomposites in the voltage window of 1.5-4.8V,[9-14] in particular, the nanorods bonded with graphene exhibits a relatively stable capacity of more than 200 mAh g^{-1} in the voltage window of 1.5-4.8V at room temperature.[10-11] Moreover, the LFS exhibits multielectron reaction during charge/discharge process at 55℃[13-14] because charge transfer become easier at higher temperature. Considering these results and our previous experiments, [7-8] we plausibly arrive at a conclusion that the continuous and fast transport of the charges (electrons and Li^+ ions) may be critical to the more than one lithium extraction/insertion in LFS material. Electrical conduction phase and nanoporous structure can help with continuous multielectron reaction in the LFS, in addition to improving rate-performances of electrodes.

An important advantage of the present synthesis of nanofibers is simple and versatile, providing a novel approach for synthesizing small-size nanofibers, which can be extended to scale-up production. This method resolves the problems of conventional processes, including low throughput and high cost, because it does not involve any complex equipment or processes such as liquid-vapor-solid growth. Hence, the resultant materials are entirely compatible with conventional slurry-coating manufacturing for lithium-ion battery electrodes.

Conclusions

We have successfully developed a convenient strategy to synthesize small-sized nanofibles by using tri-block copolymer P123 as structure direct agents. Furthermore, this kind of small-size nanofibers can construct novel three-dimensionally ordered macroporous architecture with 3D interconnected macro-mesoporous network using polystyrene colloidal crystal array as a soft-template so as to overcome the tendency of agglomeration of the nanofibers. By means of the self-limited growth of nanocrystals in the crystalline-amorphous composite structure, the LFS/C nanofibers and nanofiber-assembled three-dimensionally ordered macroporous architectures retain a good thermal stability due to limited Ostwald ripening during crystal growth. This approach is facile and cost-saving since the hierarchical macro-mesoporous composite is directly produced by means of in situ carbonization of the surfactant along with the crystallization of Li_2FeSiO_4 without using any hard templates. Such 3D interconnected macro-mesoporous architecture act as 3D channel and reservoir for liquid electrolyte and is optimal for the easy immersion and diffusion of the electrolyte, which can shorten the path lengths with less resistance for both Li+ ion diffusion and electron transport within the electrode. As a result, the hierarchical macro-mesoporous 3DOM-LFS/C-NF showed excellent performance in a fast-rate charge/discharge cycling, which demonstrated their capability in sustaining large current during battery operation. Also, this new design of insulating oxide electrode can retain the working voltage of the electrode at high rate, thus resulting in a further enhancement of energy density. Moreover, the robust structure stability facilitates the stress/strain relaxation upon prolonged cycling. These advantages lead to the excellent rate capability and ultralong-life cycling stability. This kind of nanofiber-assembled three-dimensionally ordered structure and the effective strategy can be further applied to the high-performance energy storage devices. More significantly, this soft-template method may be extended to other oxide/carbon nanofiber materials.

Acknowledgement

This work was financially supported by National Natural Science Foundation of China (No. 21473014, No. 21073021), partially supported by Cultivation Fund of the Key Scientific and Technical Innovation Project, Ministry of Education of China (No. 708084), and the Fundamental Research Funds for the Central Universities (No. 0009-2014G1311085, and No. 310831153505).

Notes and references

[a] *New Energy Materials and Device Laboratory, School of Materials Science and Engineering, Chang'an University, Xi'an, 710064, China*
Fax: 86 29 82337340; Tel: 86 29 82337350;
E-mail: donglinli@hotmail.com
xyfan@chd.edu.cn
†Electronic Supplementary Information (ESI) available: See DOI: 10.1039/b000000x/

1 Y. L. Cheah, R. V. Hagen, V. Aravindan, R. Fiz, S. Mathur, S. Madhavi, *Nano Energy*, 2013, **2**, 57-64.
2 J-W. Jung, W.-H. Ryu, J. Shin, K. Park, Il-D. Kim, *ACS Nano*, 2015, **9**, 6717-6727.
3 M. Law, L. E. Greene, J. C. Johnson, R. Saykally, P. Yang, *Nat. Mater.*, 2005, **4**, 455-459.
4 R. Dominko, *J. Power Sources*, 2008, **184**, 462-468.
5 Z. Zheng, Y. Wang, A. Zhang, T. Zhang, F. Cheng, Z. Tao, J. Chen, *J. Power Sources*, 2012, **198**, 229-235.
6 X. Y. Fan, Y.Li, J. J.Wang, L.Gou,P.Zhao, D.L.Li, L.Huang and S.G.Sun, *J. Alloys Comp.* 2010, **493**, 77-80.
7 D.Li, R.Xie, M.Tian, S.Ma, L.Gou, X.Fan, Y.Shi, H.-T.-H.Yong and L.Hao, *J. Mater. Chem. A*, 2014, **2**, 4375-4383.
8 D. Li, H.-T.-H. Yong, R. Xie, X. Fan, L.Gou, M. Tian, S. Ma, L. Hao, L. Ni, L. Duan, *RSC Adv.* 2014, **4**, 35541-35545.
9 J. Yang, X. Kang, L. Hu, X. Gong, S. Mu, *J. Mater. Chem. A*, 2014, **2**, 6870-6878..
10 J. Yang, X. Kang, D. He, A. Zheng, M. Pan, S. Mu, *J. Mater. Chem. A*, 2015, **3**, 16567-16573.
11 J. Yang, L. Hu, J. Zheng, D.He, L. Tian, S. Mu, F. Pan, *J. Mater. Chem. A*, 2015, **3**, 9601-9608.
12 X. Wu, X. Jiang, Q. Huo, Y. Zhang, *Electrochim. Acta*, 2012, **80**, 50-55.
13 T. Muraliganth, K. R. Stroukoff, A. Manthiram, *Chem. Mater.*, 2010, ***22***, 5754–5761.
14 T. Masese, C. Tassel, Y. Orikasa, Y. Koyama, H. Arai, N. Hayashi, J. Kim, T. Mori, K. Yamamoto, Y. Kobayashi, H. Kageyama, Z. Ogumi, Y. Uchimoto, *J. Phys. Chem. C*, 2015, **119**, 10206–10211.
15 Q. Wei, Q. An, D. Chen, L. Mai, S. Chen, Y. Zhao,K. Mulonda Hercule, L. Xu, A. Minhas-Khan, Q. Zhang, *Nano Lett.* 2014, **14** ,1042.
16 T. Kennedy, E. Mullane, H. Geaney, M. Osiak, C. O'Dwyer, K. M. Ryan, *Nano Lett*. 2014, **14** , 716-723
17 H. Zhou, D. Li, M. Hibino, I. Honma, *Angew. Chem. Int. Ed.* 2005, **44**, 797-802.
18 X.-Y. Fan, Y.-X. Shi, L. Gou, D.-L. Li, *Electroch. Acta*, 2014, **142**, 268-275.
19 Y. Wang, H. Xia, L. Lu, J. Lin, *ACS Nano*, 2010, **3**, 1425-1432.
20 Y. Wang, Y. Wang, D. Jia, Z. Peng, Y. Xia, G. Zheng, *Nano Lett*. 2014, **14**, 1080-1084.
21 L. Mai, X. Tian, X. Xu, L. Chang, L. Xu, *Chem. Rev.* 2014, **114**, 11828-11862.
22 J.-Y. Liao, D. Higgins, G. Lui, V. Chabot, X. Xiao, Z. Chen, *Nano Lett.* 2013, **13**, 5467-5473.
23 D.Li, M.Tian, R.Xie, Q.Li, X.Y. Fan, L.Gou,P.Zhao, S. L. Ma, Y. X. Shi, H.-T.-H.Yong, *Nanoscale*, 2014, **6**, 3302-3308.
24 H. Yoo, M. Jo, B.-S. Jin, H.-Soo Kim, J. Cho, *Adv. Energy Mater*. 2011, **1**, 347-351.
25 H. Zhang, X. Yu, P. V. Braun, *Nat. Nanotechnol.* 2011, **6**, 277-281.
26 J. H. Pikul, H. G. Zhang, J. Cho, P. V. Braun, W. P. King, Nat. Commu. 2013, **4**:1732.
27 H. Song, K.-J. Lee, K. H. Kim, S.-T. Oh, S.-K. Lee, Y.-H. Choa, *J. Nanosci. Nanotechnol.* 2010,**10**, 106-110.

Nanoscale Accepted Manuscript

This journal is © The Royal Society of Chemistry [year]

28 B. Wang, J. L. Cheng, Y. P. Wu, D. Wang, D. N. He, *Electrochem. Commun*. 2012, **23**,5-8.
29 C. Zhou, Y. Zhang,Y. Li, J. Liu, *Nano Lett.* 2013, **13**, 2078-2085.
30 K. Sun, Y. Jing, C. Li, X. Zhang, R. Aguinaldo, A. Kargar, K. Madsen, K. Banu, Y. Zhou, Y.Bando, Z. Liu, D. Wang, *Nanoscale*, 2012, **4**,1515-1521.
31 S. H.Ko, D.Lee, H. W. Kang, K. H. Nam, J. Y.Yeo, S. J. Hong, C. P. Grigoropoulos, H. J. Sung, *Nano Lett.* 2011, **11**, 666-671.
32 D. Kong , J. Luo , Y. Wang , W. Ren , T. Yu , Y. Luo , Y. Yang, C. Cheng, *Adv. Funct. Mater.* 2014, **24**, 3815-3826.
33 J.Ren, F.-F. Li, J. Lau, L. González-Urbina, S. Licht, *Nano Lett.*, **2015**, *Article ASAP*, **DOI:** 10.1021/acs.nanolett.5b02427.
34 A. M. Chockla, K. C. Klavetter, C. B. Mullins, B. A. Korgel, *Chem. Mater.*, 2012, **24** , 3738-3745.
35 C. K. Chan, H. Peng, G. Liu, K. McIlwrath, X. F. Zhang, R. A. Huggins, Y. Cui, *Nat. Nanotech.* 2008**, 3**, 31-35.
36 D. Li, H. Zhou, I. Honma, *Nat. Mater.* 2004, **3**, 65-72.
37 X. Ji, K. T. Lee, M. Monjauze, L. F. Nazar, *Chem. Commun.*, 2008, 4288-4290.
38 R. Zhang, B. Tu, D. Zhao, *Chem. Eur. J.* 2010, **16**, 9977-9981.
39 P. F. Fulvio, R.T. Mayes , X. Wang , S. M. Mahurin, J. C. Bauer, V. Presser, J. McDonough, Y. Gogotsi, S. Dai, *Adv. Funct. Mater*. 2011, **21**, 2208-2215.
40 P. Holmquiost, P. Alexandridis and B. Lindman, *J. Phys. Chem. B*, 1998, **102**, 1149-1158.
41 S.I. Nishimura, S. Hayase, R. Kanno, M. Yashima, N. Nakayama, S. H. Im, Y. T. Lim, D. J. Suh, O Ok Park, *Adv. Mater.* **2002**, *14*, 1367-1369.
42 A. Yamada, *J. Am. Chem. Soc.*, 2008, **130**, 13212-13213.
43 F. Tuinstra, J. L. Koenig, *J. Chem. Phys*. 1970, **53**, 1126-1130.
44 A.C. Ferrari, J. Robertson, *Phys Rev B*, 2000, **61**, 14095-14107.
45 A. C. Ferrari, *Solid State Commun*, 2007, **143**, 47–57.
46 T. Xing, L. H. Li, L. Hou, X. Hu, S. Zhou, R. Peter, M. Petravic, Y. Chen, *Carbon*, 2013, **57**, 515-519.
47 K. Sato, R. Saito, Y. Oyama, J. Jiang, L.G. Cancado, M.A. Pimenta, A. Jorio, Ge.G. Samsonidze, G. Dresselhaus, M.S. Dresselhaus, *Chem Phys Lett*, 2006, **42**7, 117–121.
48 A. Sadezky, H. Muckenhuber, H. Grothe, R. Niessner, U. Pöschl, *Carbon* , 2005, **43**, 1731–1742.
49 S. H. Park, Y. Xia, *Chem. Mater.*, 1998, **10**, 1745-1747.
50 D. Zhao, J. Feng, Q. Huo, N. Melosh, G. H. Fredrickson, B. F. Chmelka, G. D. Stucky, *Science,* 1998, **279**, 548-552.
51 C. Yu, B. Tian, J. Fan, G. D. Stucky, D. Zhao, *J. Am. Chem. Soc.* 2002, **124**, 4556-4557.
52 C. Rüssel, *Chem. Mater.* 200**5**, **17**, 5843-5847.
53 S. Bhattacharyya, C. Bocker, T. Heil, J. R. Jinschek, T. Höche, C. Rüssel, H. Kohl, *Nano Lett.* 2009, **9**, 2493-2496.
54 D. Li, L.Kong, L.Zhang, X.Yao, *J. Non-Cryst. Solids*, 2000, **271**,45-55.
55 D.Li, M.Tian, R.Xie, Q.Li, S.Ma, Y.Shi, F.Li, H. Lin, L.Gou, X. Y. Fan, P.Zhao, X.Wang, X.Yao, *J. Alloys Compd.* 2014, **582**, 88-95.
56 J.Y. Bai, Z. L. Gong, D. P. Lv, Y. X. Li, H. Zou, Y. Yang, *J. Mater. Chem.* 2012, **22**, 12128-12132.
57 M. Dahbi, S. Urbonaite, T. Gustafsson, *J. Power Sources*, 2012, **205**, 456– 462.
58 H. Zhou, M.-A. Einarsrud, F. Vullum-Bruer, *J. Power Sources*, 2013, **235**, 234-242.
59 M. M. Rahman, J.-Z. Wang, M. F. Hassan, S. Chou, Z. Chen, H. K. Liu, *Energy Environ. Sci*., 2011, **4**, 952-957.
60 H. Y. Gao, L. F. Jiao, W. X. Peng, G. Liu, J. Q. Yang, Q. Q. Zhao, Z. Qi, Y. C. Si, Y. J. Wang and H. T. Yuan, *Electrochim. Acta*, 2011, **56**, 9961-9967.
61 D. Yaakov, Y. Gofer, D. Aurbach, and I. C. Halalay, *J. Electrochem. Soc.* 2010, **157**, A1383-A1391.

Nanoscale Accepted Manuscript